# Atom Probe Tomography of a Cu-doped TiNiSn Thermoelectric Material: Nanoscale Structure and Optimisation of Analysis Conditions

H. He[1], J.E. Halpin[2], S.R. Popuri[3], L. Daly[1,4,5,6], J.-W.G. Bos[3], M.P. Moody[1], D.A. MacLaren[2], P.A.J. Bagot[1,5]

1 Department of Materials, University of Oxford, Parks Road, Oxford OX1 3PH, UK

2 SUPA, School of Physics and Astronomy, University of Glasgow, Glasgow G12 8QQ, UK

3 Institute of Chemical Sciences and Centre for Advanced Energy Storage and Recovery, School of Engineering and Physical Sciences, Heriot-Watt University, Edinburgh EH14 4AS, UK

4 School of Geographical and Earth Sciences, University of Glasgow, Glasgow G12 8QQ, UK

5 Australian Centre for Microscopy and Microanalysis, University of Sydney, Sydney 2006, NSW, Australia

6 Space Science and Technology Centre, School of Earth and Planetary Science, Curtin University, Bentley, 6102 WA, Australia

## Abstract

Cu-doping and crystallographic site occupations within the half-Heusler TiNiSn, a promising thermoelectric material, have been examined by Atom Probe Tomography (APT). In particular, this investigation aims to better understand the influence of atom probe analysis conditions on the measured chemical composition. Under voltage pulsing mode, atomic planes are clearly resolved and suggest an arrangement of elements in-line within the expected half-Heusler (F-43m space group) crystal structure. The Cu dopant is also distributed uniformly throughout the bulk material. For operation under laser-pulsed modes, the returned composition is highly dependent on the selected laser energy, with

high energies resulting in the measurement of excessively high absolute Ti counts at the expense of Sn and in particular Ni. High laser energies also appear to be correlated with the detection of a high fraction of partial hits, indicating non-ideal evaporation behaviour. The possible mechanisms for these trends are discussed, along with suggestions for optimal analysis conditions for these and similar thermoelectric materials.

**Keywords:** Thermoelectrics, TiNiSn, Atom Probe Tomography, half Heusler, stoichiometry, charge-state ratios

## Introduction

Thermoelectric (TE) generators are solid-state devices that can directly convert waste heat from a variety of sources into electricity, making them especially attractive materials from an energy efficiency perspective. However, their wide-scale adoption is currently impeded by the cost of often scarce materials and relatively low heat-to-electricity conversion efficiencies (He et al., 2018; Amatya & Ram, 2012). To overcome these challenges, the intermetallic materials known as half-Heusler (HH) alloys have shown considerable promise for balancing performance with commercial feasibility (Bos, 2021) . The ideal half-Heusler structure has a 1:1:1 XYZ composition and crystallises with a cubic structure. Here, X, Y and Z occupy face-centred cubic lattices that are offset by a quarter along the body diagonal of the unit cell (Graf et al., 2011). This leaves a $4^{th}$ sublattice, which is occupied in the full-Heusler structure, leading to 1:2:1 $XY_2Z$ compositions (Graf et al., 2011) . The HH alloys are semiconducting for special electron counts of 8 or 18, which is a strict requirement for good TE performance (Bos, 2021; Graf et al., 2011; Snyder & Toberer, 2008). The best current HH alloys are based on XNiSn (n-type, X = Ti, Zr, Hf), XCoSb (p-

type) and X'FeSb (p-type, X' = Nb, Ta) (Bos, 2021). These parent structures are typically heavily modified by dopants to maximise the thermoelectric figure of merit, $ZT = S^2\sigma T\kappa^{-1}$. Here, $S$ is the Seebeck coefficient, $\sigma$ the electrical conductivity and $\kappa$ the sum of the lattice ($\kappa_{lat}$) and electronic ($\kappa_{el}$) thermal conductivity. Typical compositions are $Ti_{0.5}Zr_{0.25}Hf_{0.25}NiSn_{0.99}Sb_{0.01}$, where alloying with Ti, Zr and Hf on the X-site is used to embed phonon point-defect scattering and Sb is used as a dopant to achieve the best possible trade-off between $S$, $\sigma$ and $\kappa_{el}$ (Bos, 2021). In a contrasting strategy, small amounts of Cu (0-10% occupancy) on the vacant site in TiNiSn can achieve similar optimisation and leads to promising $ZT$ = 0.6-0.8 at 800 K (Barczak et al., 2018, 2019).

In addition to point defects, the HH alloys tend to exhibit complex phase segregation effects and microstructural heterogeneities such as variations in grain chemistry or localised segregation at grain boundaries (Barczak et al., 2018). It is therefore invaluable to have an atomic-scale understanding of alloy structure in order to identify the links between material processing conditions and optimal thermoelectric performance. This requires the use of advanced microscopy techniques, ideally characterising structure and chemical distribution across multiple length-scales. Elemental analysis within electron microscopy has been used effectively to show details of Cu segregation in TiNiSn (Barczak et al., 2018) but can be difficult to apply to three-dimensional structures including precipitates and grain boundaries. Atom Probe Tomography (APT) is complementary, offering near-atomic scale characterisation of microstructures in three dimensions and with full chemical resolution. A further advantage of APT in the present case is that Cu dopant levels of a few atomic percent are at the limit of detectability for elemental analysis within electron microscopy but remain amenable to APT. To this end, a growing number of studies of thermoelectric materials using APT are appearing in the literature, demonstrating the ability of APT to offer novel insights in this field (Pei et al., 2011; Blum

et al., 2012; Biswas et al., 2012; Kim et al., 2014; Cojocaru-Mirédin et al., 2017; Liu et al., 2017; Yu et al., 2020; Bonef et al., 2019). In the current work, we explore the microstructure of a $TiNiCu_{0.1}Sn$ HH alloy (i.e. $Ti_{32.8}$-$Ni_{32.8}$-$Sn_{32.8}$-$Cu_{1.6}$). A major motivation of using APT in these alloys is to provide fully quantitative information on inter-grain chemical variations and grain boundary segregations. However, interpretation of these measurements must be built on a solid understanding of how this particular HH alloy behaves in an atom probe experiment. Understanding the influence of analysis conditions and how to optimise them is a key focus of the current study.

## Materials and Methods

$TiNiCu_{0.1}Sn$ samples were prepared using "hot pressing" of elemental powders (Alfa Aesar, all with ≥99.8% purity) and the final alloys were found to have >98% of the theoretical density. Details of the synthesis protocols, structural characterisation using x-ray diffraction and electron microscopy and thermoelectric property measurements have been presented previously. [9] Specimens for APT were prepared following the standard lift-out method (Thompson et al., 2007), using a dual-beam FEI Helios Plasma Focused Ion Beam (PFIB) instrument (University of Glasgow). Areas for lift-out targeting the bulk of the material grains were selected, using electron backscattered diffractive mapping to select grains with specific crystallographic orientations. The Xe-plasma beam typically enables production of samples more quickly than conventional Ga ion beam instruments. It also offers alternative in-situ preparation approaches currently being explored on a number of different systems (Halpin et al., 2019; El-Zoka et al., 2020; Famelton et al., 2021). Furthermore, the larger Xe ions result in a far shallower depth of beam-species implantation compared to Ga-ions, reducing contamination in the final specimens.

APT experiments were carried out on a Cameca LEAP® 5000XR instrument (University of Oxford), with specimens examined in both laser (25-100pJ) and voltage-pulsing modes (20% pulse fraction) with the stage temperature held at 50K. All datasets produced were subsequently analysed using IVAS® 3.8.4 software (Cameca).

## Results & Discussion

### Mass Spectra

For voltage-pulsing, a sub-section of ions (~2.5M) from a typical mass spectrum is shown in Fig. 1a), with peaks labelled for all 4 detected elements. In general, this alloy ran well in the atom probe under such conditions, with sufficiently high mass-resolution to resolve all isotopes. When the same material was analysed under (100pJ) laser-pulsing, the mass-resolution remained high and a drop in background noise was apparent. The detected distributions of charge states of the ions were observed to shift due to the lower standing electric field, such that no $Ti^{3+}$ ions were detected for laser pulsing and only $Ni^{1+}$ and $Cu^{1+}$ ions were noted in this mode. While a small fraction of Sn ions were singly-ionised as $Sn^{1+}$ (see inset in Fig. 1b)), the majority still evaporated as $Sn^{2+}$, which causes a mass-to-charge state overlap with nearly all $Ni^{1+}$ ion peaks. Fig. 1c) demonstrates this issue, showing a subset of the mass spectrum from b) (region marked as 'Sn/Ni *'), where only peaks that can definitively be identified as Sn, Ni (or Cu) are coloured. The four peaks marked as 'Sn/Ni' in Fig. 1c) relate to both Sn and Ni, specifically the isotopes $^{116}Sn/^{58}Ni$, $^{120}Sn/^{60}Ni$, $^{122}Sn/^{61}Ni$ and $^{124}Sn/^{62}Ni$. This complicates composition determination, particularly when assigning peaks for spatial analysis, as discussed below. The built-in peak decomposition tool within the commercially available atom probe data analysis software, IVAS®, can reliably resolve the overlaps, however there remains a clear difference between the

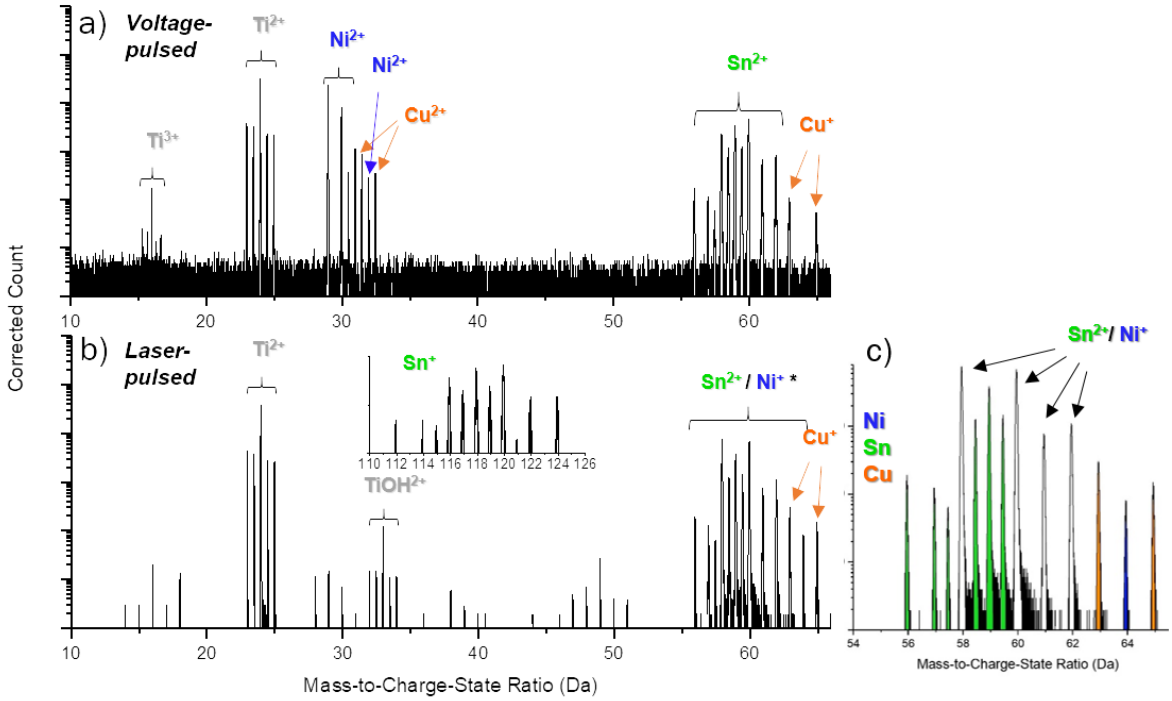


*Fig. 1 a) Mass spectrum from a) voltage-pulsed and b) laser-pulsed APT analysis of $TiNiCu_{0.1}Sn$. c) A subset of the laser-pulsed data set with unambiguous peak assignments coloured according to the legend and with overlaps between $Sn^{2+}/Ni^{+}$ ion peaks indicated.*

compositions reported by the two modes of experimental analysis. In voltage pulsing, the alloy composition is measured as (at.%) $Ti_{34.8}$-$Ni_{31.9}$-$Sn_{31.3}$-$Cu_{1.5}$, in good agreement with the nominal chemistry ($Ti_{32.8}$-$Ni_{32.8}$-$Sn_{32.8}$-$Cu_{1.6}$), while in laser mode the composition is measured as $Ti_{45.7}$-$Ni_{19.6}$-$Sn_{33.3}$-$Cu_{1.1}$, returning far more Ti at the expense of Ni. Note that the Cu content is slightly lower than expected, regardless of APT analysis mode, which suggests segregation to other parts of the microstructure. This is indeed seen in prior STEM-EDX analysis looking at grain boundaries (Barczak et al., 2018), and in ongoing APT investigations targeting these (the subject of a forthcoming study).

## Element Spatial Distributions

Before investigating the discrepancies between APT operation modes, a key motivation for the current study was to examine the detailed microstructure, focussing on the distribution of elements throughout the specimens and to assess crystallographic ordering. For this, a number of samples were analysed in voltage mode, where a clear fcc crystallographic structure was apparent in the detector hit-map data. This enabled the site-occupancy behaviour of the different species to be examined along specific crystallographic directions, along with aiding accurate spatial reconstruction of the APT datasets. Fig. 2a) shows the first of these atom maps, taken from two different specimens extracted from different locations in the same bulk ingot. For the head-on atom map shown, the central needle axis was orientated along the [001] direction. A number of distinct crystallographic poles are visible in this, as labelled with Miller indices. By cropping the reconstruction around two such pole regions orientated along the [001] and [113] directions, the localised atomic structure is visible for the two cross-sectional atom maps also in Fig. 2a). Similarly for Fig 2b), the head-on atom map from a second specimen is shown, orientated along the [111] direction from which a cross-sectional atom map can be extracted. By visual inspection, the elemental distribution in these three cross sections appears homogenous for all species, with clearly resolved planes in each instance.

The extracted maps are amenable to statistical analysis using spatial distribution maps (SDMs), plotting pair separation distances for Sn-Sn (and one set of Sn-Cu) pairs as shown for the [001] and [111]-centred reconstructions on the far left/right of Fig. 2c) and d) respectively. To aid with interpretation of these, Fig. 2c) and d) also contain schematics of the expected half-Heusler (F-43m space group) crystal structure, with sets of the {001} and {111} planes highlighted (in pink).

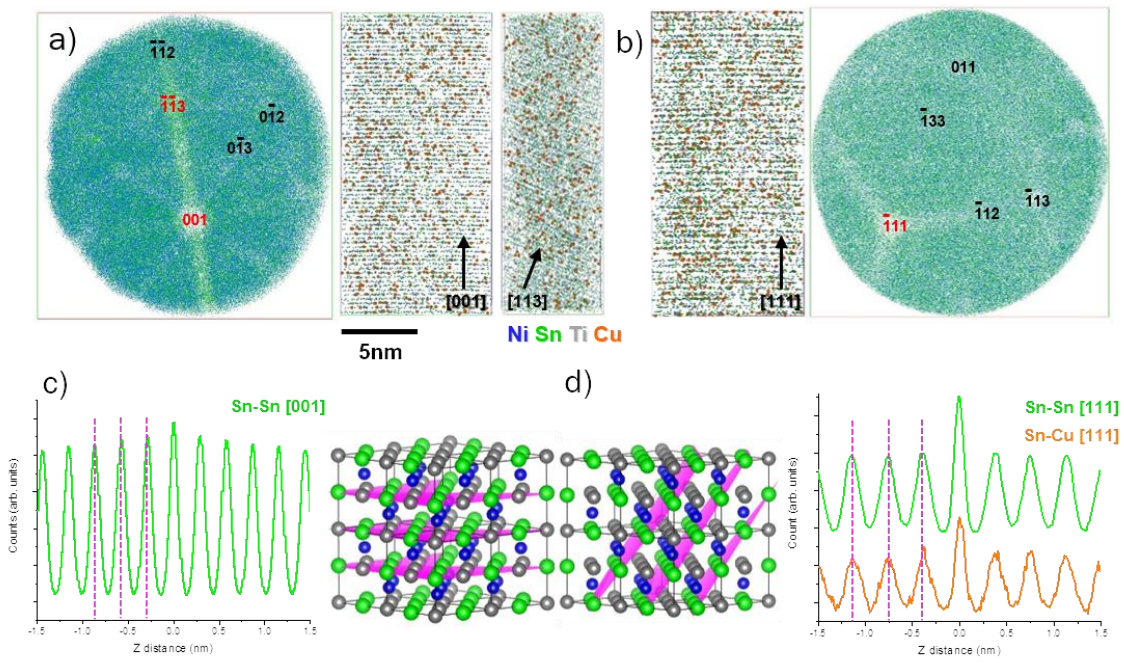


*Fig. 2 a) Atom map hit detector data from voltage-pulsed analysis of TiNiCu0.1Sn, orientated along [001] direction. Crystallographic poles are marked on the maps, from which two 20nm-long atom subsets are extracted along the [001] and [113] directions (marked in red on head-on map). b) Hit detector data for specimen orientated along [111] direction, complete with similar cross-sectional atom map extraction. Note homogenous atomic-scale structure visible in all three maps (Cu atoms enlarged for clarity). c) Spatial distribution map (SDM) for Sn-Sn along [001] direction, alongside expected crystal structure with {001} planes highlighted (pink). Note separation of planes matches (pink) vertical lines in SDM. d) SDM for Sn-Sn and Sn-Cu along [111] direction, alongside corresponding crystal structure. {111} planes again highlighted in both (pink). See text for full discussion. Crystal structures visualised using Vesta 3 (Momma & Izumi, 2011)*

The spacing of these planes is 0.297nm for {001} and 0.349nm for {111}, which corresponds very closely to the peak separations in the experiment SDMs (dotted vertical pink lines) along both directions. Finally, the consistent, non-oscillating peak heights in these demonstrate that the Sn atoms are completely mixed as expected, in-line with the model, while in Fig. 2d) the additional Sn-Cu SDM similarly reveals no site-occupancy preference for the Cu atoms; all other combinations of SDM pairs (not shown here) produced near identical results. While there may be slight blurring of sequential ion positions in the atom probe due to differences in element ion evaporation fields (Gault et al., 2012), overall the data convincingly shows there is no obvious clustering of Cu, and the elemental distribution appears homogeneous for all species. As further support for this, there is also no evidence for significant Ti/Sn inversion from Rietveld analysis of neutron powder diffraction data with interstitials the lowest energy defects in the XNiSn HH alloys (Downie et al., 2015).

## Analysis Conditions – Voltage vs. Laser Pulsing

For laser-pulsed analysis, an excess of Ti at the expense of Ni was observed in many experiments. This bias towards Ti often appeared more pronounced near the start of an experiment, gradually shifting towards, but not reaching, the expected 1:1:1 metal ratios for Ti:Ni:Sn. A degree of surface segregation and oxidation of Ti has previously been observed in related TiNiSn samples (Webster et al., 2019) but diffusion of Ti is not expected within the experimental timescale at a temperature of 50K nor can explain the differences between APT operation modes. To confirm that apparent Ti enrichment was, indeed, an artefact of laser operation and not a genuine compositional variation within the microstructure, one single sample was run sequentially for three separate experiments in laser, voltage then laser modes again. The datasets from this are shown in Fig. 3, as a

series of consecutive atom maps in Fig. 3a) and corresponding 1D analysis profiles below in Fig. 3b).

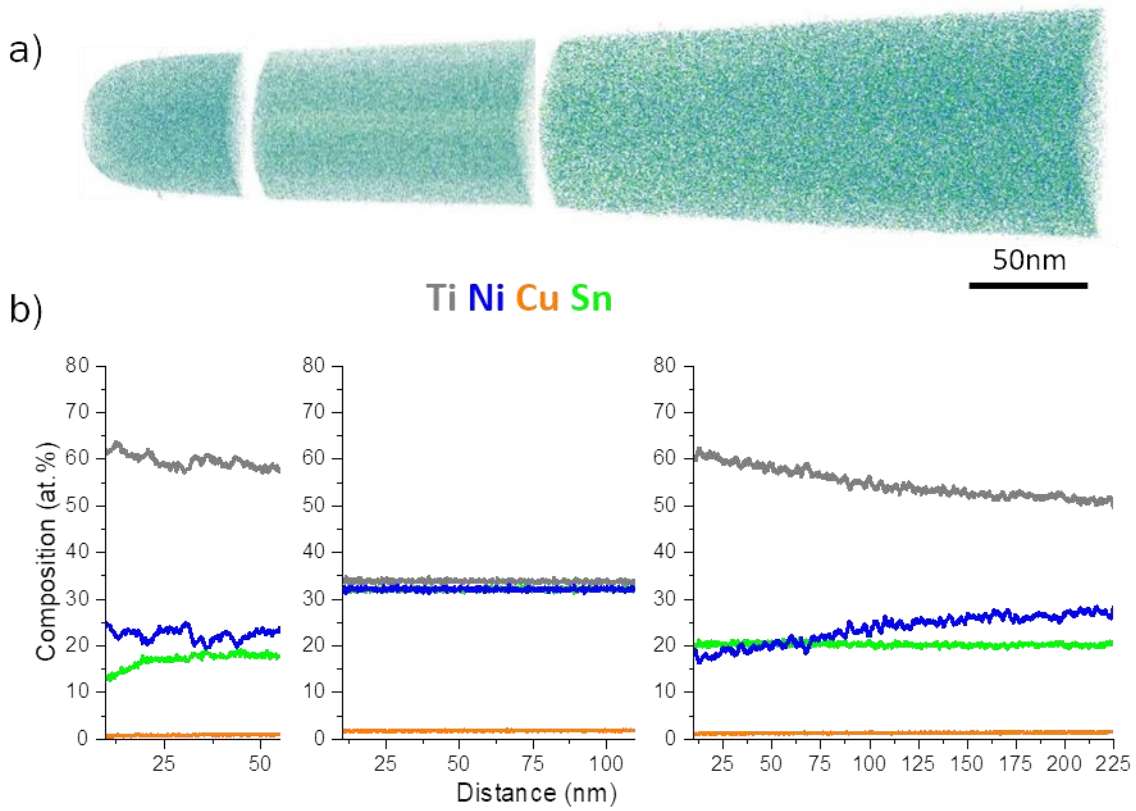


*Fig. 3 a) Atom maps from single TiNiCu$_{0.1}$Sn specimen successively run in laser, voltage, then laser-pulsed modes on LEAP 5000XR system. b) 1D concentration profiles along the tip axis corresponding to atom maps in a). The nominal material stoichiometry is confirmed for voltage mode analysis (middle), while both laser mode analyses show excess Ti and a secondary depth-dependence of composition. 20% voltage pulsing/100pJ laser pulsing used, with a stage temperature of 50K.*

The voltage-pulsed run data (centre panel of Fig. 3) was reconstructed with the aid of the crystallographic planes apparent in the atom map, yielding initial and final tip-radii, which aided accurate reconstruction of the laser-pulsed runs either side. In total, 52M ions were

collected, and while the microstructure was free of any nano-preciptates, it is clear from Fig. 3b) that both laser runs report off-composition, while the voltage mode data is consistent with expected 1:1:1 Ti:Ni:Sn stoichiometry. The comparison leads to the conclusion that such materials should, if possible, be examined using a voltage-pulsed approach, in-line with that used by other researchers on a related thermoelectric material (Bonef et al., 2019). However, the option of utilising laser-pulsing is desirable, particularly to boost experiment yields and for targeted regions such as grain-boundaries where considerable effort is invested in workflow stages of specimen preparation. Therefore the erroneously-high Ti contents seen in Fig. 3 are worth examining further.

Taking the voltage-pulse mode as providing a more accurate measure of composition, the origin of artefacts in the laser-pulse data was assessed. The first parameter targeted was the laser-pulse energy, as the effects of this on composition are well-documented in a wide-range of materials (Devaraj et al., 2013; Pedrazzini et al., 2017; Hans & Schneider, 2019; Chang et al., 2019; Morris et al., 2019). A series of experiments was undertaken to explore the effect of laser pulse energy on alloy composition, shown in Fig. 4 for the three major elements. Laser energies varied from 25-100pJ, all plotted alongside data from a voltage-pulsed run ('0pJ'). The horizontal dotted lines indicate the nominal content of each element, while the points show (averaged) bulk composition data combined across a number of datasets. These indicate that while the returned Sn content is comparatively stable and representative across changing laser energies, at 50pJ the reported Ti level rises at the expense of Ni, with the divergence attaining a maximum value above 70pJ. Despite the clear influence of the laser pulse energy on the data obtained, we did not observe any sign of localised heating effects across the tip apex as a result of one side directly facing the beam; the (x-y) hit-map data was homogeneous over the whole surface, even at the highest laser pulse energies.

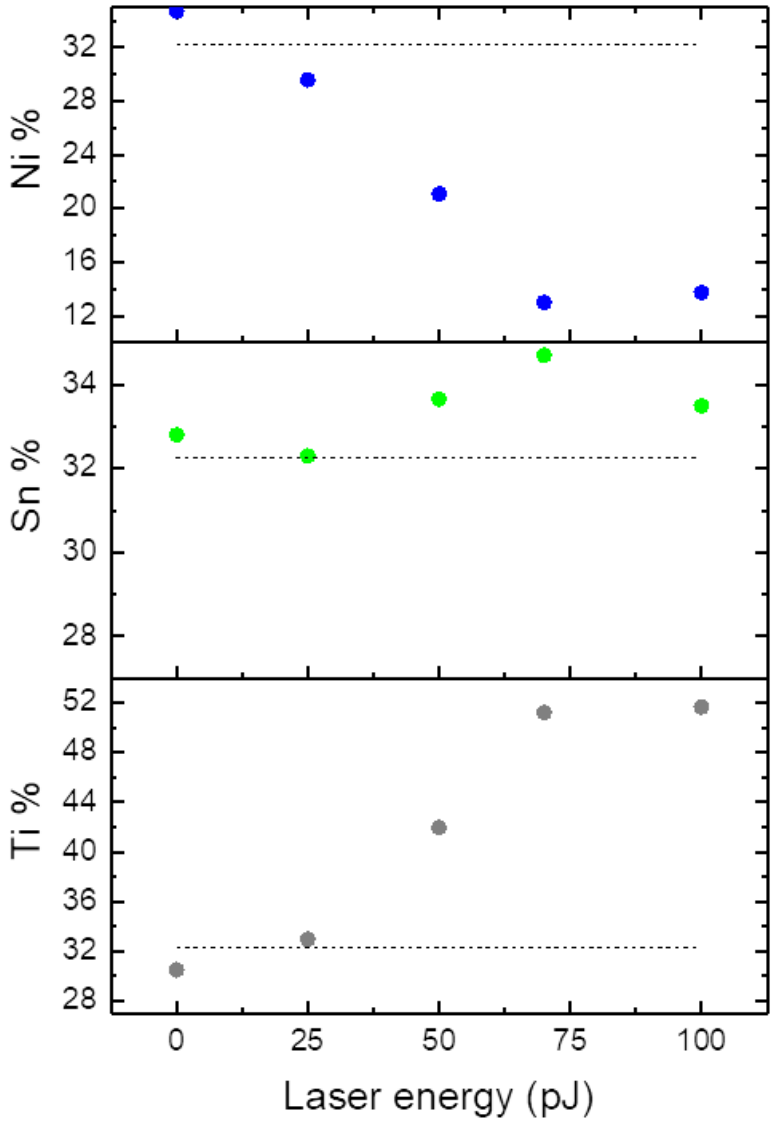


*Fig. 4 Composition dependence of main alloying elements (Ni, Sn and Ti) on laser pulse energy.*

The extent of the discrepancy between the nominal and recorded compositions is somewhat surprising, as alloys containing these elements have been extensively studied by a number of APT groups using comparable laser pulse energies. Even in materials with known systematic issues limiting the return of accurate compositions, such as oxide

superconductors (Pedrazzini et al., 2017), the deviations from expected stoichiometry when varying laser-pulse energies are not as dramatic as seen in the current study.

To understand how the electric field conditions at the specimen apex may be contributing to the trends, we examined the charge state ratios (CSRs) for selected ion species, which allow an estimate of the electric field to be made using the Kingham curves (Kingham, 1982). In this case Ni is the most appropriate element to study, as both $Ni^{2+}$ and $Ni^{+}$ are present in the spectra, with the relative quantities of each being strongly dependent on analysis conditions (see Fig. 1).

Extracting the Ni CSRs across the full range of analysis conditions, plots of CSR varying with laser energy (Fig. 5a)) and Ni content (Fig. 5b)) were generated. As expected, running at higher laser pulse energies (for constant 0.3% evaporation rate) markedly reduces the standing field at the specimen apex. This lowers the fraction of higher charge state ($Ni^{2+}$) ions detected, causing a drop in log CSR as shown in Fig. 5a). The plot of Ni content versus log CSR has more scattered data but there is still a clear trend for strongly negative CSR values (when the applied field is low) resulting in detecting fewer Ni ions than expected from the known stoichiometry. The dotted vertical line in Fig. 5b) marks the field value where the Kingham curves predict a 50:50 $Ni^{2+}$:$Ni^{+}$ ratio (approximately 24V/nm); this appears to be a suitable empirical threshold for determining appropriate running conditions, corresponding to a reported Ni content of ~30 at.% for all CSR values at or above this value.

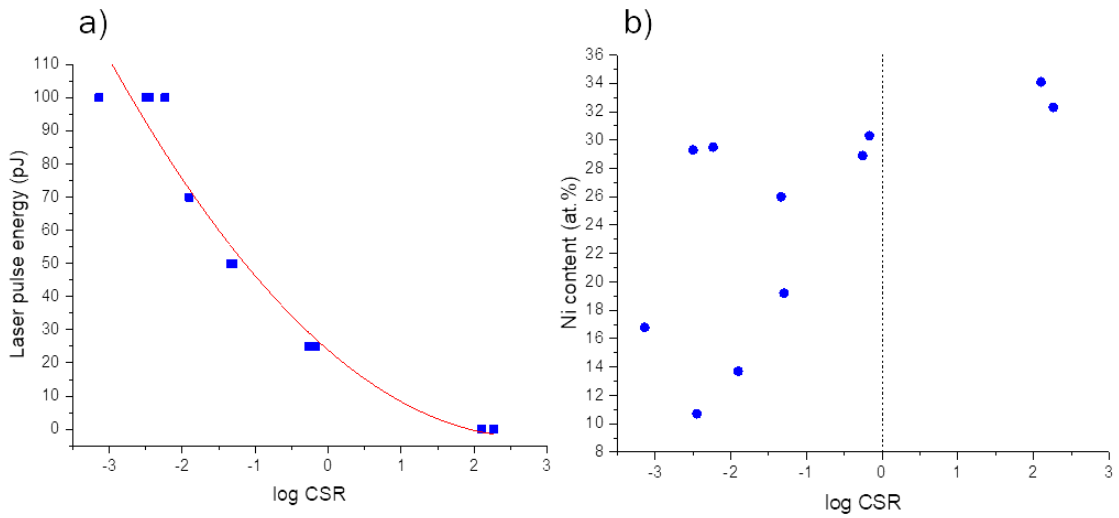


*Fig. 5. Relationship between ($log_{10}$) charge-state-ratios of detected ($Ni^{2+}/Ni^{+}$) ions and a) laser-pulse energy, b) measured Ni content over all $TiNiCu_{0.1}Sn$ specimens analysed. The red line in a) is a parabolic fit to guide the eye. The dotted line in b) denotes a 50:50 $Ni^{2+}$:$Ni^{+}$ ratio at ~24 V/nm, as predicted elsewhere (Kingham, 1982). $Ni^{2+}/Ni^{+}$ charge state ratio measurements are based on the ratio of 58Ni2+ to 58Ni+ ions recorded in each mass spectrum.*

While this analysis outlines suitable analysis conditions for running these materials, it is of interest to explore the likely underlying mechanisms in more depth. The calculated evaporation fields ($F_n$) (using the image hump model) for the three major elements in their dominant charge states are: $Ti^{2+}$ 26V/nm, $Ni^{+}$ 35V/nm and $Sn^{2+}$ 23V/nm (Miller et al., 1996). Thus, Ni has the highest activation barrier by some measure among the three elements, however consideration of the resulting field evaporation behaviour predicted by these differences does not account for the observations.

At constant temperature (i.e. during voltage-pulsed analysis), the evaporation rate has a very strong dependence on the field at the sample tip. This can cause severe issues analysing materials with species having differing $F_n$ values, as the element with the highest evaporation field displays the strongest dependence on the field strength (Miller et al.,

1996). Higher $F_n$ value species likely evaporate when the pulse is applied, whereas lower $F_n$ value elements can evaporate between pulses. In practice, the detector only records hits that can be directly correlated from the pulse, so the composition becomes biased towards higher $F_n$ elements. There is no evidence of this occurring in the current study for any of the voltage-pulsed runs, indicating the pulse-fraction used (20%) was sufficient to evaporate all ion species. Furthermore, a mechanism based on bias in favour of higher $F_n$ elements is unlikely to be behind the erroneous laser-pulsed data, as temperature, not field, is the variable used to control evaporation, and the dependence of the evaporation rate on temperature is much weaker than on field (Miller et al., 1996).

An alternative line of investigation emerges on inspection of the detector statistics, in the form of 'partial hits'. The term partial hit in APT refers to a detector event in which an ion impact is recorded, but does not register on one (or more) of the six delay-line detector wires. This can be caused by the impacting ion having too low kinetic energy, leading to an insufficient electron cascade at the multichannel plate (MCP) (Oberheide et al., 1997). For any ions species detected as partials, there is higher probability that other identical ions do not register on the detector at all, resulting in a deficiency in the reported composition. Thus the fraction of partial hits can be utilised as a metric for data quality. To show this, the Ni/Ti ratio is plotted against the total fraction of partial hits (as a percentage of all events) across all collected datasets in Fig. 6. Examining this, results are broadly split into two groups: those with more typical, acceptably low values (around 5% or less), and those with around 20% or more. It is clear that high partial hits are closely correlated with relative loss of Ni. All of these Ni-deficient runs were carried out using high (50-100pJ) laser pulse energies.

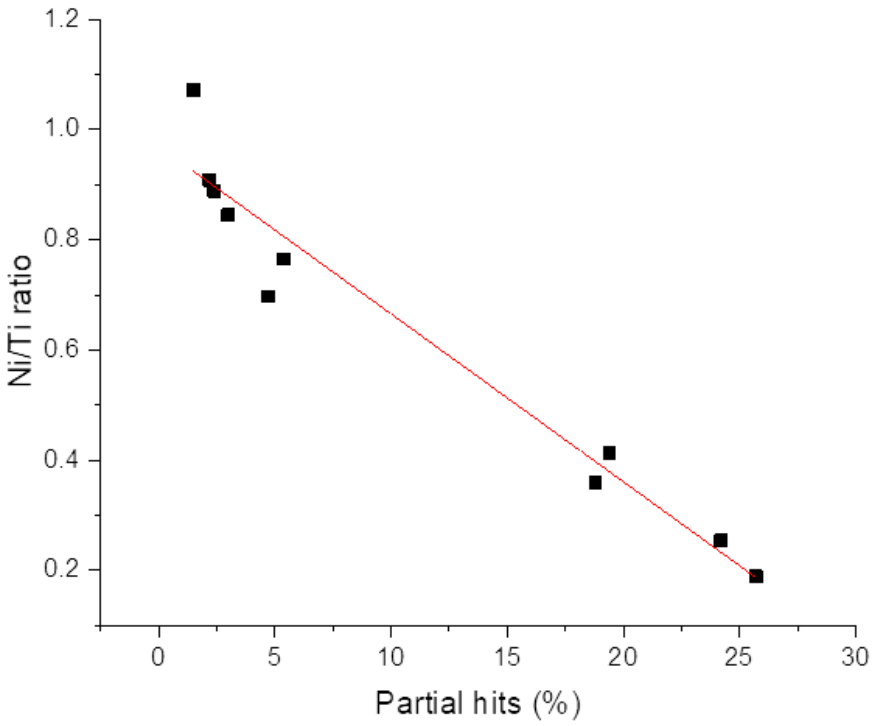


*Fig. 6. Plot of calculated overall Ni:Ti ratio as a function of reported detector partial hits (%) for all datasets.*

Further evidence that Ni is preferentially lost in this manner is shown by extracting composition data arising from partial hits alone. For the experiment with the highest proportion of partial hits (25.7%), the Ni content from partial hits alone is 13%, vs. 10.7% when measured using all data. Similarly for the next two most affected experiments (24.2% and 19.4% partial hits), the Ni contents are respectively 13.8% (partials) vs. 13.0% (all), and 20.0% (partials) vs. 19.4% (all). Thus there is a small but measurable bias against Ni ions that are not being detected in the laser-pulsed experiments. Also of note is that the proportion of multiple hits in laser-pulsed experiments was universally low; typically ~1-5%, vs. 18-20% for voltage-pulsed runs. This is consistent with a strong absorption of the laser beam, breaking any ion clusters that can typically result in detecting high levels of multiple hits (Müller et al., 2011; Thuvander et al., 2013)

There is also a secondary, more minor effect of the composition drifting with increasing depth during a laser-pulsed run, as seen from the gradual reduction of Ti and increase of Ni in Fig. 3b). For the second, longer laser-pulsed analysis in this figure, the partial hit fraction can be sampled throughout the reconstruction depth, and this is shown in Fig. 7a). These start high, then rapidly fall off with increasing depth into the specimen. The start of this experiment also coincides to when the composition is least accurate, with an apparent low Ni/very high Ti content (Fig. 3b)). The partial hit fraction is therefore again serving as an indicator of inappropriate running conditions. The charge state ratios for all three main alloying elements were also sampled throughout this run, shown in Fig. 7 b)-d). For Ni, the log CSR values are strongly negative throughout, rising but never reaching near the empirical 50:50 $Ni^{2+}$:$Ni^{+}$ target. Similarly, for Ti and Sn the CSRs shift towards the higher ($2^{+}$) charge state, all of which indicates that the electric field is rising throughout the run. This is somewhat unexpected; conventionally, as a tip becomes blunter during the course of an experiment, the field-of-view gradually increases, resulting in a higher density of hits on the detector. As the detection rate is held constant (0.3%) by the software controlling the atom probe instrument, the applied field must therefore be decreased. However, in laser-pulsed mode, as the tip becomes progressively blunt, the volume of material at the apex heated by the laser becomes larger. In turn, this means the apex cools more quickly, and thus a higher electric field is required to cause evaporation, as seen in the data here.

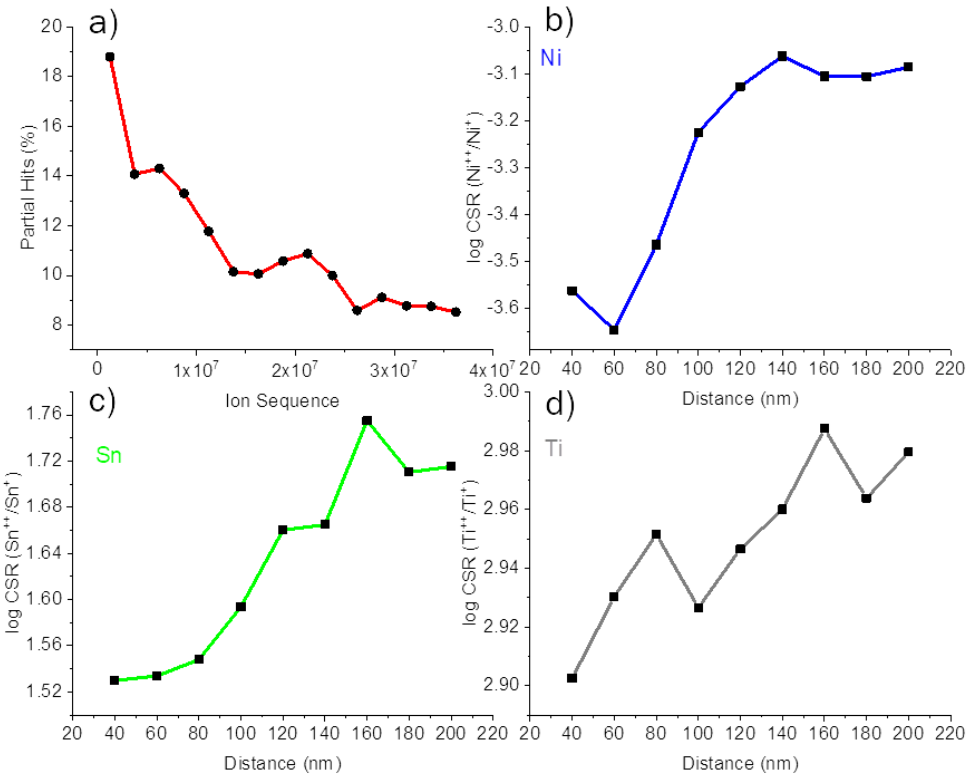


*Fig. 7 a) Partial hit percentage recorded on $TiNiCu_{0.1}Sn$ run in laser-pulsed mode (100pJ) as function of specimen depth (ion sequence) b)-d) ($log_{10}$) charge-state-ratios for Ni, Sn and Ti (++:+) as function of specimen depth for same specimen as in a).*

The (lattice) thermal conductivity, $\kappa_{lat}$, of the Heusler alloys likely plays an important role in the atom probe experiment, as materials with high thermal conductivity can readily transfer heat from the laser pulse through even small cross-sections of tip material into the specimen shank. Conversely, a less conductive material (i.e. more insulating) will tend to retain heat localised at the sample tip, affecting the field evaporation behaviour, particularly for narrow specimen cross-sections. Typical thermal conductivity values for engineering alloys commonly analysed by APT using nickel or titanium range from 10-100 $Wm^{-1}K^{-1}$, significantly higher than the quoted range for various Cu-doped TiNiSn alloys of

around 4-4.5 $Wm^{-1}K^{-1}$ (Barczak et al., 2018). Thus, it is perhaps not surprising that the latter behave quite differently from expectations under laser-pulsed APT analysis. It is also feasible that the issues regarding high partial hits are at least partly related to thermal conductivity; the mass spectra for the two runs having highest partial hit fractions in Fig. 6 had noticeably wider peaks, which is indicative of greater thermal energy retention at the specimen apex and consequent off-pulse evaporation.

For developing working devices using thermoelectric materials, driving $\kappa_{lat}$ to lower values is highly desirable to maximise the thermoelectric figure of merit, *ZT,* which is a generic goal for many materials in this application. *ZT* values are also frequently used for comparing different thermoelectric materials (Amatya & Ram, 2012). Indeed the addition of the trace levels of Cu in this alloy lowers $\kappa_{lat}$, along with improving electronic properties, therefore it is likely that researchers using APT to characterise the microstructure of thermoelectrics will need to carefully account for this material property.

## Conclusions

A detailed study of the bulk near atomic-scale microstructure of a $TiNiCu_{0.1}Sn$ half-Heusler alloy has been carried out by APT. Quantitative data from these materials appears particularly sensitive to the chosen instrument analysis conditions, with laser-pulsing causing significant deviation from the expected stoichiometry. This is attributed to the low thermal conductivity of these alloys. By running at suitably low laser pulse energies of ≤25pJ however, applicable to current LEAP® 5000 systems utilising 355nm laser illumination, accurate quantification can be obtained. It is also recommended to pay close attention to performance metrics such as the number of partial hits. Abnormally high levels

of such (>20%) likely indicate the alloy is not field evaporating in a suitable manner conducive to accurate quantification.

When optimal spatial reconstructions are desired, voltage-mode pulsing enables atomic-scale features to be readily resolved, in addition to returning accurate compositional data. For this alloy, bulk regions are seen to be homogenous in composition, with the Cu dopant distributed uniformly throughout the crystal matrix. Such calibration studies are important to be able to probe potential changes in the composition within different regions and grains in such materials, particularly when attempting to optimise the level of trace additions such as Cu to maximise thermoelectric performance.

## Acknowledgements

The Oxford Atom Probe facility is funded by EPSRC (EP/M022803/1) and the Glasgow plasma focused ion beam system was funded by EPSRC grant EP/P001483/1. Thermoelectric materials were developed under joint EPSRC grants EP/N017218/1 and EP/N01717X/1. Jaspreet Singh (University of Oxford) and Ty Prosa (Cameca Instruments) are thanked for helpful discussions.

## References


AMATYA, R. & RAM, R. J. (2012). Trend for thermoelectric materials and their earth abundance. *Journal of Electronic Materials* **41**, 1011–1019.

BARCZAK, S. A., HALPIN, J. E., BUCKMAN, J., DECOURT, R., POLLET, M., SMITH, R. I., MACLAREN, D. A. & BOS, J. W. G. (2018). Grain-by-Grain Compositional Variations and Interstitial Metals - A New Route toward Achieving High Performance in Half-Heusler Thermoelectrics. *ACS Applied Materials and Interfaces* **10**, 4786–4793.

BARCZAK, S. A., QUINN, R. J., HALPIN, J. E., DOMOSUD, K., SMITH, R. I., BAKER, A. R., DON, E., FORBES, I., REFSON, K., MACLAREN, D. A. & BOS, J. W. G. (2019). Suppression of thermal conductivity without impeding electron mobility in n-type XNiSn half-Heusler thermoelectrics †.

BISWAS, K., HE, J., BLUM, I. D., WU, C. I., HOGAN, T. P., SEIDMAN, D. N., DRAVID, V. P. & KANATZIDIS, M. G. (2012). High-performance bulk thermoelectrics with all-scale hierarchical architectures. *Nature* **489**, 414–418.

BLUM, I. D., ISHEIM, D., SEIDMAN, D. N., HE, J., ANDROULAKIS, J., BISWAS, K., DRAVID, V. P. & KANATZIDIS, M. G. (2012). Dopant distributions in PbTe-based thermoelectric materials. *Journal of Electronic Materials* **41**, 1583–1588.

BONEF, B., HARRINGTON, S. D., PENNACHIO, D. J., SPECK, J. S. & PALMSTRØM, C. J. (2019). Nanometer scale structural and compositional inhomogeneities of half-Heusler CoTi1-xFexSb thin films. *Journal of Applied Physics* **125**.

BOS, J. W. G. (2021). Recent development in half-Heusler thermoelectric materials. In *Thermoelectric Energy Conversion*, Funahashi, R. (Ed.), pp. 125–142. Woodhead Publishing.

Chang, Y. H., Mouton, I., Stephenson, L., Ashton, M., Zhang, G. K., Szczpaniak, A., Lu, W. J., Ponge, D., Raabe, D. & Gault, B. (2019). Quantification of solute deuterium in titanium deuteride by atom probe tomography with both laser pulsing and high-voltage pulsing: influence of the surface electric field. *New Journal of Physics* **21**, 053025. https://iopscience.iop.org/article/10.1088/1367-2630/ab1c3b.

Cojocaru-Mirédin, O., Abdellaoui, L., Nagli, M., Zhang, S., Yu, Y., Scheu, C., Raabe, D., Wuttig, M. & Amouyal, Y. (2017). Role of Nanostructuring and Microstructuring in Silver Antimony Telluride Compounds for Thermoelectric Applications. *ACS Applied Materials and Interfaces* **9**, 14779–14790.

Devaraj, A., Colby, R., Hess, W. P., Perea, D. E. & Thevuthasan, S. (2013). Role of Photoexcitation and Field Ionization in the Measurement of Accurate Oxide Stoichiometry by Laser-Assisted Atom Probe Tomography.

Downie, R. A., Barczak, S. A., Smith, R. I. & Bos, J. W. G. (2015). Compositions and thermoelectric properties of XNiSn (X = Ti, Zr, Hf) half-Heusler alloys. *J. Mater. Chem. C* **3**, 10534. www.rsc.org/MaterialsC.

El-Zoka, A. A., Kim, S. H., Deville, S., Newman, R. C., Stephenson, L. T. & Gault, B. (2020). Enabling near-atomic-scale analysis of frozen water. *arXiv* 1–12.

Famelton, J. R., Hughes, G. M., Williams, C. A. & Barbatti, C. (2021). Xenon plasma Focussed Ion Beam preparation of an Al-6XXX alloy sample for Atom Probe Tomography including analysis of an α -Al ( Fe , Mn ) Si dispersoid. *submitted to Microscopy & Microanalysis*.

Gault, B., Moody, M. P., Cairney, J. M. & Ringer, S. P. (2012). *Atom Probe Microscopy*. Springer.

Graf, T., Felser, C. & Parkin, S. S. P. (2011). Simple rules for the understanding of

Heusler compounds. *Progress in Solid State Chemistry* **39**, 1–50.

HALPIN, J. E., WEBSTER, R. W. H., GARDNER, H., MOODY, M. P., BAGOT, P. A. J. & MACLAREN, D. A. (2019). Ultramicroscopy An in-situ approach for preparing atom probe tomography specimens by xenon plasma-focussed ion beam. *Ultramicroscopy* **202**, 121–127. https://doi.org/10.1016/j.ultramic.2019.04.005.

HANS, M. & SCHNEIDER, J. M. (2019). On the chemical composition of TiAlN thin films - Comparison of ion beam analysis and laser-assisted atom probe tomography with varying laser pulse energy. *Thin Solid Films* **688**, 137251. https://doi.org/10.1016/j.tsf.2019.04.026.

HE, R., SCHIERNING, G. & NIELSCH, K. (2018). Thermoelectric Devices: A Review of Devices, Architectures, and Contact Optimization. *Advanced Materials Technologies* **3**.

KIM, Y. J., BLUM, I. D., HE, J., KANATZIDIS, M. G., DRAVID, V. P. & SEIDMAN, D. N. (2014). Three-Dimensional Atom-Probe Tomographic Analyses of Lead-Telluride Based Thermoelectric Materials. *Journal of Materials* **66**, 2288–2297.

KINGHAM, D. R. (1982). The post-ionization of field evaporated ions: a theoretical explanation of multiple charge states. *Surface Science* **116**, 273–301.

LIU, R., CHEN, H., ZHAO, K., QIN, Y., JIANG, B., ZHANG, T., SHA, G., SHI, X., UHER, C., ZHANG, W. & CHEN, L. (2017). Entropy as a Gene-Like Performance Indicator Promoting Thermoelectric Materials. *Advanced Materials* **29**, 1702712. www.advancedsciencenews.com.

MILLER, M. K., CEREZO, A., HETHERINGTON, M. G. & SMITH, G. D. W. (1996). *Atom Probe Field Ion Microscopy*. Oxford University Press.

MOMMA, K. & IZUMI, S. (2011). VESTA 3 for three-dimensional visualization of crystal,

volumetric and morphology data. *Journal of Applied Crystallography* **44**, 1272–1276.

MORRIS, R. J. H., CUDUVALLY, R., MELKONYAN, D., ZHAO, M., VAN DER HEIDE, P. & VANDERVORST, W. (2019). Atom probe of GaN/AlGaN heterostructures: The role of electric field, sample crystallography and laser excitation on quantification. *Ultramicroscopy* **206**. https://doi.org/10.1016/j.ultramic.2019.112813.

MÜLLER, M., SAXEY, D. W., SMITH, G. D. W. & GAULT, B. (2011). Some aspects of the field evaporation behaviour of GaSb. *Ultramicroscopy* **111**, 487–492.

OBERHEIDE, J., WILHELMS, P. & ZIMMER, M. (1997). New results on the absolute ion detection efficiencies of a microchannel plate. *Measurement Science and Technology* **8**, 351–354.

PEDRAZZINI, S., LONDON, A. J., GAULT, B., SAXEY, D., SPELLER, S., GROVENOR, C. R. M., DANAIE, M., MOODY, M. P., EDMONDSON, P. D. & BAGOT, P. A. J. (2017). Nanoscale Stoichiometric Analysis of a High-Temperature Superconductor by Atom Probe Tomography. *Microscopy and Microanalysis* **23**, 414–424.

PEI, Y., LENSCH-FALK, J., TOBERER, E. S., MEDLIN, D. L. & SNYDER, G. J. (2011). High thermoelectric performance in PbTe due to large nanoscale Ag 2Te precipitates and La doping. *Advanced Functional Materials* **21**, 241–249.

SNYDER, G. J. & TOBERER, E. S. (2008). Complex thermoelectric materials. *Nature Materials* **7**, 105–114.

THOMPSON, K., LAWRENCE, D., LARSON, D. J., OLSON, J. D., KELLY, T. F. & GORMAN, B. (2007). In situ site-specific specimen preparation for atom probe tomography. *Ultramicroscopy* **107**, 131–139.

THUVANDER, M., KVIST, A., JOHNSON, L. J. S., WEIDOW, J. & ANDRÉN, H. O. (2013). Reduction of multiple hits in atom probe tomography. *Ultramicroscopy* **132**, 81–85.

WEBSTER, R. W. H., HALPIN, J. E., POPURI, S. R., BOS, J.-W. G. & MACLAREN, D. A. (2019). Spontaneous formation of nanostructures during pulsed laser deposition of epitaxial half-Heusler TiNiSn on MgO(001) ARTICLES YOU MAY BE INTERESTED IN. **7**, 13206. https://doi.org/10.1063/1.5052361.

YU, Y., ZHOU, C., ZHANG, S., ZHU, M., WUTTIG, M., SCHEU, C., RAABE, D., SNYDER, G. J., GAULT, B. & COJOCARU-MIRÉDIN, O. (2020). Revealing nano-chemistry at lattice defects in thermoelectric materials using atom probe tomography. *Materials Today* **32**, 260–274. https://doi.org/10.1016/j.mattod.2019.11.010.